Check for updates

Hyperspectral absorption and backscattering coefficients of bulk water retrieved from a combination of remote-sensing reflectance and attenuation coefficient

JUNFANG LIN,[1,4] ZHONGPING LEE,[1,5] MICHAEL ONDRUSEK,[2] AND XIAOHAN LIU[3]

[1]*School for the Environment, University of Massachusetts Boston, Boston, MA, USA*
[2]*NOAA/NESDIS/STAR/SOCD, College Park, Greenbelt, MD, USA*
[3]*State Key Laboratory of Lake Science and Environment, Nanjing Institute of Geography and Limnology, Chinese Academy of Sciences, Nanjing, China*
[4]*Junfang.Lin@umb.edu*
[5]*Zhongping.Lee@umb.edu*

Abstract: Absorption (a) and backscattering (b_b) coefficients play a key role in determining the light field; they also serve as the link between remote sensing and concentrations of optically active water constituents. Here we present an updated scheme to derive hyperspectral a and b_b with hyperspectral remote-sensing reflectance (R_{rs}) and diffuse attenuation coefficient (K_d) as the inputs. Results show that the system works very well from clear open oceans to highly turbid inland waters, with an overall difference less than 25% between these retrievals and those from instrument measurements. This updated scheme advocates the measurement and generation of hyperspectral a and b_b from hyperspectral R_{rs} and K_d, as an independent data source for cross-evaluation of *in situ* measurements of a and b_b and for the development and/or evaluation of remote sensing algorithms for such optical properties.

References and links

1. R. W. Preisendorfer, M. Stark, I. Sneddon, and S. Ulam, *Radiative Transfer on Discrete Spaces* (Pergamon, 1965).
2. C. D. Mobley, *HydroPol Mathematical Documentation: Invariant Imbedding Theory for the Vector Radiative Transfer Equation* (Sequoia Scientific Inc., 2014).
3. C. D. Mobley, *Light and Water: Radiative Transfer in Natural Waters* (Academic, 1994).
4. H. R. Gordon, "Absorption and scattering estimates from irradiance measurements: Monte Carlo simulations," Limnol. Oceanogr. **36**, 769–777 (1991).
5. Z. Lee, K. L. Carder, and R. A. Arnone, "Deriving inherent optical properties from water color: a multiband quasi-analytical algorithm for optically deep waters," Appl. Opt. **41**(27), 5755–5772 (2002).
6. J. R. V. Zaneveld, "An asymptotic closure theory for irradiance in the sea and its inversion to obtain the inherent optical properties," Limnol. Oceanogr. **34**, 1442–1452 (1989).
7. Z. Lee, *Remote Sensing of Inherent Optical Properties: Fundamentals, Tests of Algorithms, and Applications* (International Ocean-Colour Coordinating Group, 2006).
8. D. McKee, A. Cunningham, and S. Craig, "Semi-empirical correction algorithm for AC-9 measurements in a coccolithophore bloom," Appl. Opt. **42**(21), 4369–4374 (2003).
9. R. Röttgers, D. McKee, and S. B. Woźniak, "Evaluation of scatter corrections for ac-9 absorption measurements in coastal waters," Methods in Oceanography **7**, 21–39 (2013).
10. R. Ma, D. Pan, H. Duan, and Q. Song, "Absorption and scattering properties of water body in Taihu Lake, China: backscattering," Int. J. Remote Sens. **30**, 2321–2335 (2009).
11. W. H. Slade and E. Boss, "Spectral attenuation and backscattering as indicators of average particle size," Appl. Opt. **54**(24), 7264–7277 (2015).
12. T. Kostadinov, D. Siegel, and S. Maritorena, "Retrieval of the particle size distribution from satellite ocean color observations," Journal of Geophysical Research: Oceans **114**, C09022 (2009).
13. Z. Lee, K. Du, and R. Arnone, "A model for the diffuse attenuation coefficient of downwelling irradiance," Journal of Geophysical Research: Oceans **110**, C02016 (2005).

14. S. Sathyendranath and T. Platt, "The spectral irradiance field at the surface and in the interior of the ocean: a model for applications in oceanography and remote sensing," Journal of Geophysical Research: Oceans **93**, 9270–9280 (1988).

15. Z. Lee, K. L. Carder, and K. Du, "Effects of molecular and particle scatterings on the model parameter for remote-sensing reflectance," Appl. Opt. **43**(25), 4957–4964 (2004).

16. H. R. Gordon, O. B. Brown, R. H. Evans, J. W. Brown, R. C. Smith, K. S. Baker, and D. K. Clark, "A semianalytic radiance model of ocean color," J. Geophys. Res., D, Atmospheres **93**, 10909–10924 (1988).

17. H. R. Gordon and G. C. Boynton, "Radiance-irradiance inversion algorithm for estimating the absorption and backscattering coefficients of natural waters: vertically stratified water bodies," Appl. Opt. **37**(18), 3886–3896 (1998).

18. H. Loisel and D. Stramski, "Estimation of the inherent optical properties of natural waters from the irradiance attenuation coefficient and reflectance in the presence of Raman scattering," Appl. Opt. **39**(18), 3001–3011 (2000).

19. A. Morel and B. Gentili, "Diffuse reflectance of oceanic waters. II Bidirectional aspects," Appl. Opt. **32**(33), 6864–6879 (1993).

20. A. Morel and B. Gentili, "Diffuse reflectance of oceanic waters. III. Implication of bidirectionality for the remote-sensing problem," Appl. Opt. **35**(24), 4850–4862 (1996).

21. Z. Lee, C. Hu, S. Shang, K. Du, M. Lewis, R. Arnone, and R. Brewin, "Penetration of UV-visible solar radiation in the global oceans: Insights from ocean color remote sensing," Journal of Geophysical Research: Oceans **118**, 4241–4255 (2013).

22. Z. Lee, S. Shang, K. Du, J. Wei, and R. Arnone, "Usable solar radiation and its attenuation in the upper water column," Journal of Geophysical Research: Oceans **119**, 1488–1497 (2014).

23. A. Morel and H. Loisel, "Apparent optical properties of oceanic water: dependence on the molecular scattering contribution," Appl. Opt. **37**(21), 4765–4776 (1998).

24. J. Berwald, D. Stramski, C. D. Mobley, and D. A. Kiefer, "Influences of absorption and scattering on vertical changes in the average cosine of the underwater light field," Limnol. Oceanogr. **40**, 1347–1357 (1995).

25. C. D. Mobley, "Polarized reflectance and transmittance properties of windblown sea surfaces," Appl. Opt. **54**(15), 4828–4849 (2015).

26. T. J. Petzold, *Volume Scattering Functions for Selected Ocean Waters* (Scripps Institution of Oceanography La Jolla Ca Visibility Lab, 1972).

27. W. W. Gregg and K. L. Carder, "A simple spectral solar irradiance model for cloudless maritime atmospheres," Limnol. Oceanogr. **35**, 1657–1675 (1990).

28. B. G. Mitchell, "Algorithms for determining the absorption coefficient for aquatic particulates using the quantitative filter technique (QFT)," Proc. SPIE **1320**, 137–148 (1990).

29. C. S. Yentsch, "Measurement of visible light absorption by particulate matter in the ocean," Limnol. Oceanogr. **7**, 207–217 (1962).

30. J. Wei, Z. Lee, and S. Shang, "A system to measure the data quality of spectral remote ensing reflectance of aquatic environments," Journal of Geophysical Research: Oceans **121**, 8189–8207 (2016).

31. R. Snyder and J. Dera, "Wave-induced light-field fluctuations in the sea," J. Opt. Soc. Am. **60**, 1072–1079 (1970).

32. R. M. Pope and E. S. Fry, "Absorption spectrum (380-700 nm) of pure water. II. Integrating cavity measurements," Appl. Opt. **36**(33), 8710–8723 (1997).

33. Z. Lee, J. Wei, K. Voss, M. Lewis, A. Bricaud, and Y. Huot, "Hyperspectral absorption coefficient of "pure" seawater in the range of 350–550 nm inverted from remote sensing reflectance," Appl. Opt. **54**, 546–558 (2015).

34. A. Morel, "Optical properties of pure water and pure sea water," Optical aspects of oceanography **1**, 22 (1974).

35. Z. P. Lee, K. Du, K. J. Voss, G. Zibordi, B. Lubac, R. Arnone, and A. Weidemann, "An inherent-optical-property-centered approach to correct the angular effects in water-leaving radiance," Appl. Opt. **50**(19), 3155–3167 (2011).

36. H. R. Gordon, and A. Y. Morel, *Remote Assessment of Ocean Color for Interpretation of Satellite Visible Imagery: A Review* (Springer-Verlag, 1983).

37. P. J. Werdell and S. W. Bailey, "An improved in-situ bio-optical data set for ocean color algorithm development and satellite data product validation," Remote Sens. Environ. **98**, 122–140 (2005).

38. Y. Huot, C. A. Brown, and J. J. Cullen, "New algorithms for MODIS sun-induced chlorophyll fluorescence and a comparison with present data products," Limnol. Oceanogr. Methods **3**, 108–130 (2005).

39. C. S. Roesler and E. Boss, "Spectral beam attenuation coefficient retrieved from ocean color inversion," Geophys. Res. Lett. **30**, 1468 (2003).

40. E. Boss, and C. Roesler, "Over constrained linear matrix inversion with statistical selection," Remote Sensing of Inherent Optical Properties: Fundamentals, Tests of Algorithms, and Applications, IOCCG, Dartmouth, NS, Canada, IOCCG Rep **5** (2006).

41. S. A. Garver and D. A. Siegel, "Inherent optical property inversion of ocean color spectra and its biogeochemical interpretation: 1. Time series from the Sargasso Sea," Journal of Geophysical Research: Oceans **102**, 18607–18625 (1997).

42. E. Boss, M. Picheral, T. Leeuw, A. Chase, E. Karsenti, G. Gorsky, L. Taylor, W. Slade, J. Ras, and H. Claustre, "The characteristics of particulate absorption, scattering and attenuation coefficients in the surface ocean; Contribution of the Tara Oceans expedition," Methods in Oceanography **7**, 52–62 (2013).

43. D. McKee, J. Piskozub, R. Röttgers, and R. A. Reynolds, "Evaluation and improvement of an iterative scattering correction scheme for in situ absorption and attenuation measurements," J. Atmos. Ocean. Technol. **30**, 1527–1541 (2013).
44. C. C. Moore, E. J. Bruce, W. Pegau, and A. D. Weidemann, "WET Labs ac-9: Field calibration protocol, deployment techniques, data processing, and design improvements," in *Ocean Optics XIII*(1997), pp. 725–730.
45. X. Liu, Y. Zhang, Y. Yin, M. Wang, and B. Qin, "Wind and submerged aquatic vegetation influence bio-optical properties in large shallow Lake Taihu, China," J. Geophys. Res. Biogeosci. **118**, 713–727 (2013).
46. Y. Zhang, Y. Yin, X. Liu, Z. Shi, L. Feng, M. Liu, G. Zhu, Z. Gong, and B. Qin, "Spatial-seasonal dynamics of chromophoric dissolved organic matter in Lake Taihu, a large eutrophic, shallow lake in China," Org. Geochem. **42**, 510–519 (2011).
47. A. Morel, "Optical modeling of the upper ocean in relation to its biogenous matter content (case I waters)," Journal of Geophysical Research: Oceans (1978–2012) **93**, 10749– 10768 (1988).
48. G. C. Boynton and H. R. Gordon, "Irradiance inversion algorithm for absorption and backscattering profiles in natural waters: improvement for clear waters," Appl. Opt. **41**(12), 2224–2227 (2002).
49. G. C. Boynton and H. R. Gordon, "Irradiance inversion algorithm for estimating the absorption and backscattering coefficients of natural waters: Raman-scattering effects," Appl. Opt. **39**(18), 3012–3022 (2000).
50. J. R. V. Zaneveld, J. C. Kitchen, and C. C. Moore, "Scattering error correction of reflection-tube absorption meters," in *Ocean Optics XII* (International Society for Optics and Photonics, 1994), pp. 44–56.
51. E. Boss, W. H. Slade, M. Behrenfeld, and G. Dall'Olmo, "Acceptance angle effects on the beam attenuation in the ocean," Opt. Express **17**(3), 1535–1550 (2009).
52. D. McKee and A. Cunningham, "Evidence for wavelength dependence of the scattering phase function and its implication for modeling radiance transfer in shelf seas," Appl. Opt. **44**(1), 126–135 (2005).
53. D. McKee, J. Piskozub, and I. Brown, "Scattering error corrections for in situ absorption and attenuation measurements," Opt. Express **16**(24), 19480–19492 (2008).
54. E. Leymarie, D. Doxaran, and M. Babin, "Uncertainties associated to measurements of inherent optical properties in natural waters," Appl. Opt. **49**(28), 5415–5436 (2010).
55. D. Doxaran, E. Leymarie, B. Nechad, A. Dogliotti, K. Ruddick, P. Gernez, and E. Knaeps, "Improved correction methods for field measurements of particulate light backscattering in turbid waters," Opt. Express **24**(4), 3615–3637 (2016).
56. Wetlab, "WET Labs ECO BB User's Guide " (2017).
57. E. Boss, W. S. Pegau, W. D. Gardner, J. R. V. Zaneveld, A. H. Barnard, M. S. Twardowski, G. Chang, and T. Dickey, "Spectral particulate attenuation and particle size distribution in the bottom boundary layer of a continental shelf," Journal of Geophysical Research: Oceans **106**, 9509–9516 (2001).
58. R. A. Maffione and D. R. Dana, "Instruments and methods for measuring the backward-scattering coefficient of ocean waters," Appl. Opt. **36**(24), 6057–6067 (1997).
59. J. Wollschläger, M. Grunwald, R. Röttgers, and W. Petersen, "Flow-through PSICAM: a new approach for determining water constituents absorption continuously," Ocean Dyn. **63**, 761–775 (2013).
60. D. Stramski, "Fluctuations of solar irradiance induced by surface waves in the Baltic," Bull. Pol. Acad. Sci. Earth Sci. **34**, 333–344 (1986).
61. G. Zibordi, D. D'Alimonte, and J.-F. Berthon, "An evaluation of depth resolution requirements for optical profiling in coastal waters," J. Atmos. Ocean. Technol. **21**, 1059–1073 (2004).
62. D. D'Alimonte, E. B. Shybanov, G. Zibordi, and T. Kajiyama, "Regression of in-water radiometric profile data," Opt. Express **21**(23), 27707–27733 (2013).
63. M. Darecki, D. Stramski, and M. Sokólski, "Measurements of high-frequency light fluctuations induced by sea surface waves with an Underwater Porcupine Radiometer System," Journal of Geophysical Research: Oceans **116**, C00H09 (2011).
64. J. Wei, M. R. Lewis, R. Dommelen, C. J. Zappa, and M. S. Twardowski, "Wave-induced light field fluctuations in measured irradiance depth profiles: A wavelet analysis," Journal of Geophysical Research: Oceans **119**, 1344–1364 (2014).
65. H. R. Gordon, "Can the Lambert-Beer law be applied to the diffuse attenuation coefficient of ocean water?" Limnol. Oceanogr. **34**, 1389–1409 (1989).
66. C. D. Mobley, L. K. Sundman, and E. Boss, "Phase function effects on oceanic light fields," Appl. Opt. **41**(6), 1035–1050 (2002).
67. M. Tzortziou, J. R. Herman, C. L. Gallegos, P. J. Neale, A. Subramaniam, L. W. Harding, and Z. Ahmad, "Bio-optics of the Chesapeake Bay from measurements and radiative transfer closure," Estuar. Coast. Shelf Sci. **68**, 348–362 (2006).
68. A. Tonizzo, M. Twardowski, S. McLean, K. Voss, M. Lewis, and C. Trees, "Closure and uncertainty assessment for ocean color reflectance using measured volume scattering functions and reflective tube absorption coefficients with novel correction for scattering," Appl. Opt. **56**, 130–146 (2017).
69. M. Twardowski, X. Zhang, S. Vagle, J. Sullivan, S. Freeman, H. Czerski, Y. You, L. Bi, and G. Kattawar, "The optical volume scattering function in a surf zone inverted to derive sediment and bubble particle subpopulations," Journal of Geophysical Research: Oceans **117** (2012).
70. H. R. Gordon, M. R. Lewis, S. D. McLean, M. S. Twardowski, S. A. Freeman, K. J. Voss, and G. C. Boynton, "Spectra of particulate backscattering in natural waters," Opt. Express **17**(18), 16192–16208 (2009).

1. Introduction

The inherent optical properties (IOPs) include absorption (a, m^{-1}), scattering (b, m^{-1}), and beam attenuation (c, m^{-1}) coefficients of water, which determine the magnitude and spectral signature of the light field in water. The apparent optical properties (AOPs), such as the irradiance reflectance (R, dimensionless), the remote sensing reflectance (R_{rs}, sr^{-1}), and the diffuse attenuation coefficient of downwelling irradiance (K_d, m^{-1}), are connected to the IOPs via the radiative transfer equation [1–3]. To simplify the calculations, various models have been developed to provide quick, and more straightforward cause-effect, relationships between IOPs and AOPs. Subsequently, IOPs can be retrieved from these AOPs through various algorithms [4–6].

During the past decades, many commercial hydrologic optical instruments (e.g., ACS or AC9 from WET Labs Inc., HS6 from HOBI Labs Inc.) have been widely employed in the field to obtain *in situ* values of IOPs. These instruments not only facilitate the study of IOPs of water but also provide "ground truths" for evaluation of the IOPs derived from inversion algorithms [7]. However, many limitations still remain in the operation of these instruments. First, it is found that uncertainties of these measurements sometimes can be very large (e.g., uncertainties of ACS measurements resulted from pure-water calibration and scattering corrections could reach more than 30% [8, 9]). Further, current backscattering (b_b, m^{-1}) meters (e.g., HS6) have difficulty in obtaining reliable measurements in some complex waters (e.g., Lake Taihu, China) because of an inappropriate sigma-correction [10]. And, there is still no instrument available yet that can measure hyperspectral b_b, which could provide valuable information on particle size and its composition [11, 12]. Therefore, it is useful and important to find alternative ways to obtain reliable hyperspectral a and b_b *in situ*.

Currently, commercial spectroradiometers can provide simultaneous hyperspectral measurements of radiance and irradiance in the upper water column, which can be used to obtain AOPs such as R, R_{rs}, and K_d. Previous studies have also shown that these AOPs are well related to a and b_b [13–16]. Based on this knowledge, Gordon and Boynton [17] used radiance-irradiance profiles to estimate a and b_b in stratified waters. To simplify the calculations, Loisel and Stramski [18] developed a model to retrieve hyperspectral a, b and b_b from the combination of R just beneath the sea surface and K_d of the first optical depth. The limitation of this scheme is that most instruments provide measurements of R_{rs}, not R. It is thus necessary to convert R_{rs} to R via some empirical models [19, 20] if one is to apply this model for global measurements. The conversion factor between R_{rs} and R is not a constant though, thus extra uncertainties could be introduced into the estimates of a and b_b if this scheme is applied.

In this paper, with an updated model for R_{rs} and the K_d model presented in Lee et al. [21], an updated scheme to derive hyperspectral a and b_b with hyperspectral (350-700 nm, ~2 nm step) R_{rs} and K_d as inputs is presented, where values of hyperspectral a and b_b spectra were obtained in oceanic and turbid inland waters. These estimates were further compared with available *in situ* measurements from commercial instruments to check constancy. Furthermore, limitations and sources of uncertainties associated with both strategies for *in situ* a and b_b are discussed.

2. Data

2.1 Hydrolight simulations

As in many studies [13, 22–24], a series of radiative transfer simulations (Table 1) were carried out with Hydrolight (http://www.sequoiasci.com). The simulation data are used to (1) obtain model parameters of remote sensing reflectance for the geometry angles not included in the look-up table (LUT) presented in Lee et al. [15], and (2) to evaluate the updated scheme for derivation of a and b_b from purely radiative-transfer simulated K_d and R_{rs} to check model consistency. Note that the current Hydrolight implements a scalar (unpolarized)

version of invariant imbedding calculations, thus some uncertainties could be introduced. In addition, the sea surface modeling for wave elevation and slope could also introduce some potential uncertainties [25].

Table 1. List of data sets.

Data set	Measurements (or Simulations)	N
Hydrolight	$-E_d$(z), $-L_u$(z)	81 spectra with Raman, 81 spectra without Raman
NOMAD	$-K_d$, $-R_{rs}$, $-a(\lambda)$, $-b_b(\lambda)$	746 spectra
VIIRS2014	$-E_d$(z), $-L_u$(z), $-a(\lambda)$, $-b_b(\lambda)$	21 stations
Lake Taihu	$-E_d$(z), $-R_{rs}(\lambda)$, $-a(\lambda)$	113 spectra

For these simulations, class-1 IOP models (classic case-1 option in Hydrolight) were adopted; chlorophyll-a concentration was set to a wide range from 0.01 to 50 mg/m^3 (0.01, 0.05, 0.1, 1, 2, 5, 10, 20, 50 mg/m^3); wavelengths were set in a range of 360 − 700 nm (20 nm step); the sun was positioned at a range of 0° − 80° from zenith (10° step); and an averaged phase function for particle scattering (Petzold [26]) was used. A wind speed of 5 m/s was assumed, and the sky was set cloud free. For all simulations, geophysical depths ranged from 0 − 200 m (with 1 m depth resolution for 0 − 20 m range and 5 m depth resolution for the 20 − 200 m range, respectively). The skylight was simulated by RADTRAN developed by Gregg and Carder [27]. The contributions of fluorescence from chlorophyll-a or colored-dissolved organic matter were not included in this study. For each IOP case, two simulations were carried out separately (with and without Raman). The data set without Raman scattering was used for the modeling of sub-surface remote sensing reflectance (r_{rs}, sr^{-1}), and the one with Raman was used for the application/evaluation of the R_{rs}-K_d scheme.

2.2 Field measurements

To evaluate the new scheme, measurements from a wide range of aquatic environments were used, which include measurements collected in oceanic, coastal, and highly turbid inland waters (Fig. 1).

Set one: A data set, including concurrent IOPs (a and b_b), R_{rs} and K_d, was obtained from the NASA bio-Optical Marine Algorithm Data set (NOMAD), which covers a K_d(490) range from ~0.016 to ~4.6 m^{-1}. The total absorption coefficients were derived from measurements of the two major components: absorption coefficient of suspended particles and colored dissolved organic matter (CDOM), where the particle absorption was measured with quantitative filter-pad technique [28, 29]. The measurements of the spectral b_b were obtained using HOBI Labs Inc. HS6, or WET Labs ECO-BB or ECO-VSF. The concurrent measurements of R_{rs} and K_d were acquired from profile measurements of upwelling radiance and downwelling irradiance, respectively. A scheme of quality control for R_{rs} was also conducted following the method of Wei et al. [30], and here we only used R_{rs} values with a quality assurance score higher than 0.7.

Set two: Data collected from NOAA VIIRS ocean color validation cruise in 2014 (21 stations during 10 days). Profiles of downwelling irradiance (E_d, w/m^2/nm) and upwelling radiance (L_u, w/m^2/nm/sr) were collected with a Satlantic hyperspectral profiler, which is equipped with up to 135 bands covering a wavelength range from ~352 nm to 800 nm. The radiometry sensors were calibrated a few days before the cruise. The r_{rs} was calculated as the ratio of L_u(0$^-$) to E_d(0$^-$) just below the water surface, which were obtained via extrapolation of measured L_u(z) and E_d(z) vertical profiles, respectively. The spectral K_d was calculated by a nonlinear fitting of E_d(z) between 0$^-$ and z$_{10\%}$, which is the depth where E_d(z) is 10% of E_d(0$^-$). To reduce the impact of wave-focusing effect [31] on derived R_{rs} and K_d, multiple casts of profile measurements were collected for each station (normally 4-8 casts for each station). In

addition, the non-water absorption coefficients were measured by two ACS (WETLabs Inc.) meters, where the two ACS instruments were mounted inside the same profiling cage. The pure-water calibration was carried out on the first day and the middle of this cruise. The scattering correction was conducted with the method (Eq. (4) of Röttgers et al. [9]. Finally, the total absorption coefficients were calculated by the sum of non-water absorption coefficients and pure seawater absorption coefficients with the values of later taken from Pope and Fry [32] and Lee et al. [33]. The backscattering coefficients of seawater were measured by an ECO-BB7FL2 (WETLabs Inc.). The dark offsets were obtained by covering the detectors with electrical tape on the last day of the cruise. The values of pure seawater backscattering coefficients were taken from Morel [34].
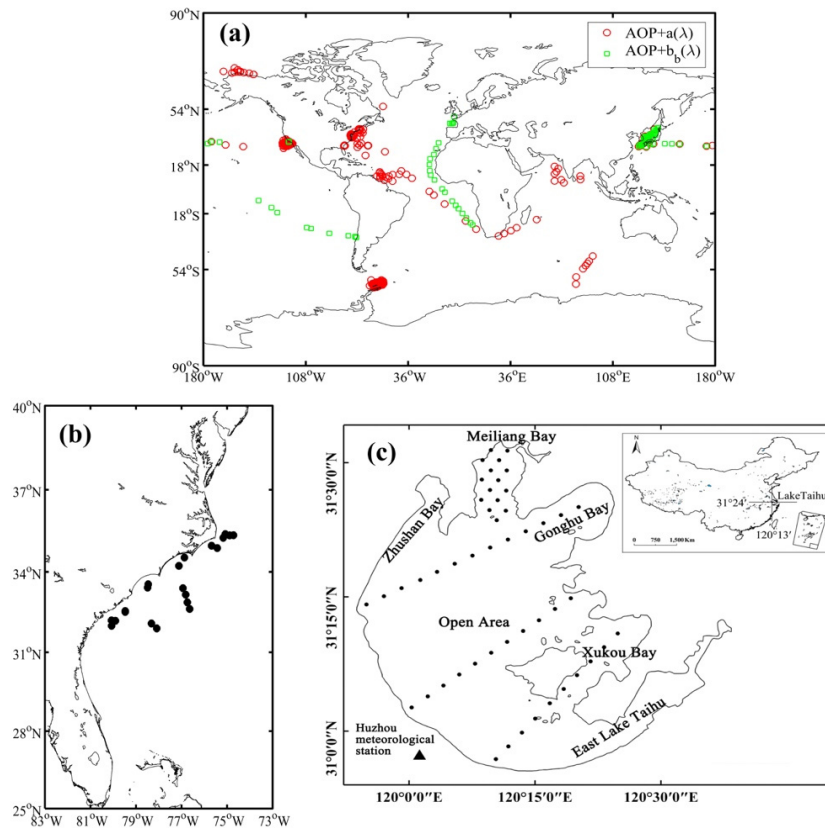
Fig. 1. Locations of field measurements for (a) NOMAD data set, (b) VIIRS2014 data set, and (c) Taihu Lake data set.

Set three: A data set obtained from Lake Taihu, China, which is a typical turbid shallow lake with significant spatial and seasonal variation of optical properties. A total of 113 concurrent measurements (a, R_{rs} and K_d) were compiled, where the $K_d(490)$ value ranged from ~2.0 to ~20.7 m^{-1}. The particulate absorption was measured using the quantitative filter-pad technique. The above-water measurement of R_{rs} was collected with an ASD (Analytical Spectral Devices) field spectrometer (Analytical Devices, Inc, Boulder, CO). Separately, an SAM 8180 sensor (TriOS) was used to measure the E_d at different depths between 0 to 1 m with a depth resolution of ~5 cm. The spectral K_d was then calculated by a nonlinear fitting of $E_d(z)$ between 0^- and $z_{10\%}$.

3. Methods

3.1 Two-term r_{rs} model

Table 2. Parameters of r_{rs} model (Eq. 2).

θ_v	φ_v	x_0	x_1	x_2	x_3	y_0	y_1	y_2	y_3	y_4	y_5
0°	0°	0.113	−0.00074	0.021	0.0086	12.36	0.056	−0.0007	5.32	−0.062	0.00045
40°	135°	0.117	−0.00037	0.019	−0.0009	13.16	−0.036	0.00047	3.97	−0.024	0.00019

In this study, we adopted the two-term r_{rs} model in Lee et al. [15] to link r_{rs} with IOPs, which is expressed as

$$r_{rs}(\Omega) = \left(G_0^w(\Omega) + G_1^w(\Omega) \cdot \frac{b_{bw}}{a+b_b} \right) \frac{b_{bw}}{a+b_b} + \left(G_0^p(\Omega) + G_1^p(\Omega) \cdot \frac{b_{bp}}{a+b_b} \right) \frac{b_{bp}}{a+b_b} \quad (1)$$

with a and b_b the total absorption and backscattering coefficients of the bulk water; while $b_b = b_{bw} + b_{bp}$, and the subscript w and p represent water and particles, respectively. Here Ω represents the sun-sensor angular geometry for r_{rs}. $G_0^w, G_1^w, G_0^p, G_1^p$ are model parameters that are functions of sun angle (θ_s) and viewing angles (θ_v and φ_v) [15]. A LUT for discrete sun-sensor angular geometry has been developed in Lee et al. [35]. To effectively determine model parameters for sun angles not included in the LUT and to obtain a smooth transition among the sun angles, we here express the model parameters ($G_0^w, G_1^w, G_0^p, G_1^p$) of each view geometry (θ_v and φ_v), respectively, as a function of sun angle.

$$G_0^w(\theta_s) = x_0 e^{x_1 \left(\frac{\theta_s}{\theta_{s0}} \right)} \quad (2.1)$$

$$G_1^w(\theta_s) = x_2 e^{x_3 \left(\frac{\theta_s}{\theta_{s0}} \right)} \quad (2.2)$$

$$G_0^p(\theta_s) = \left(y_0 + y_1 \left(\frac{\theta_s}{\theta_{s0}} \right) + y_2 \left(\frac{\theta_s}{\theta_{s0}} \right)^2 \right)^{-1} \quad (2.3)$$

$$G_1^p(\theta_s) = \left(y_3 + y_4 \left(\frac{\theta_s}{\theta_{s0}} \right) + y_5 \left(\frac{\theta_s}{\theta_{s0}} \right)^2 \right)^{-1} \quad (2.4)$$

where θ_{s0} is a reference sun angle and fixed here at 30°. The values of model parameters (x_{0-3} and y_{0-5}, Table 2) were obtained by a nonlinear fitting between parameters ($G_0^w, G_1^w, G_0^p, G_1^p$) and θ_s via Eqs. (2.1) − (2.4). Note that the values of both θ_v and φ_v are 0° when applied to profiler measurements ($L_u(z)$ and $E_d(z)$).

3.2 Model for K_d

We employed the latest K_d model as presented in Lee et al. [21], where K_d is expressed as

$$K_d = (1 + m_0 \cdot \theta_s) \cdot a + \left(1 - \gamma \cdot \frac{b_{bw}}{b_b} \right) \cdot m_1 \cdot \left(1 - m_2 \cdot e^{-m_3 \cdot a} \right) \cdot b_b \quad (3)$$

The model parameters (m_{0-3} and γ) are presented in Lee et al. [21]. Note that this model can be used to estimate K_d from ultraviolet to the visible bands.

3.3 Steps to estimate a and b_b

As described by Eqs. (1) and (3), both r_{rs} and K_d are functions of a and b_b; therefore, for any wavelength having measurements of both r_{rs} and K_d, there are just two unknowns, thus it is straightforward to calculate a and b_b from the two equations. Note that θ_s is obtained according to the time and location (longitude and latitude) of the field measurements. In addition, a correction of contribution from Raman scattering was also applied to R_{rs} following the approach of Lee et al. [21], and the conversion between r_{rs} and R_{rs} is given by the following equation

$$r_{rs} = \frac{R_{rs}}{0.52 + 1.7 R_{rs}}$$ (4)

Therefore, as long as values of $r_{rs}(\lambda)$ and $K_d(\lambda)$ are provided, $a(\lambda)$ and $b_b(\lambda)$ can be calculated straightforwardly. Note that it is not straightforward to correct the contributions from chlorophyll fluorescence, therefore retrievals of IOPs in the longer wavelengths (around 683 nm) in field-measured data could contain larger uncertainties.

4. Evaluation of the derived IOPs

4.1 Self-consistency test
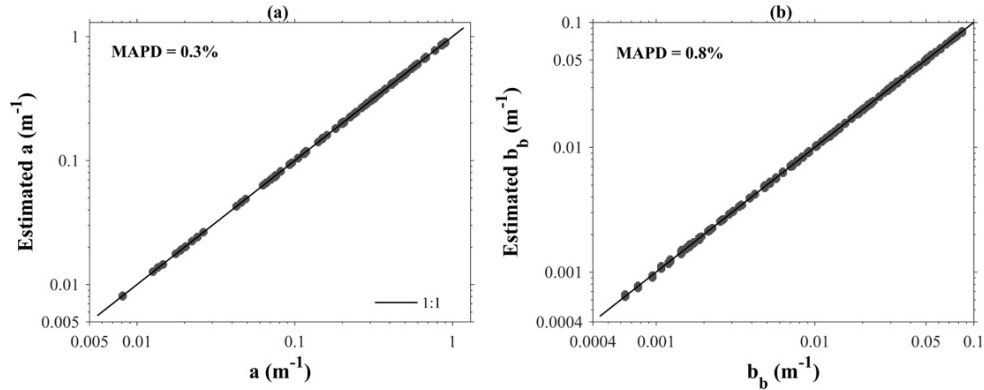
Fig. 2. A self-consistency test of Hydrolight simulated data showing the reliability of retrieved a&b_b with the updated scheme (all wavelengths included, x-axis representing Hydrolight-input a and b_b, and the y-axis representing estimated a and b_b from R_{rs}&K_d).

With data obtained from Hydrolight simulations (Raman scattering included), a self-consistency test was first conducted and the results are shown in Fig. 2. The impact of Raman scattering on R_{rs} was first corrected with the approach of Lee et al. [21]. Note that a and b_b (from 400 nm to 700 nm) are also the input parameters for the Hydrolight simulations, which are further compared with a and b_b estimated from R_{rs} and K_d that are calculated from the simulated light field. It is found that the mean absolute percentage difference (MAPD) is very small (< 1% on average), which indicates that errors in the derived a and b_b resulted from the model formulation and model parameters employed for r_{rs} and K_d are extremely small. The MAPD here is defined as

$$MAPD = \frac{1}{n} \sum_{i=1}^{n} \left| \frac{x_k - x_m}{x_k} \right|$$ (5)

where x_k is a known value and x_m is a modeled value. To understand the error propagation in the scheme, a test was further conducted with ± 5% or ± 10% errors included in R_{rs} or K_d. The results are shown in Table 3. It is found that generally the error in derived a is primarily resulted from K_d, while the error in derived b_b is contributed by both R_{rs} and K_d, with the

compound error generally less than ~11% for a and less than ~20% for b_b for ± 10% errors in both R_{rs} and K_d.

Table 3. Impact of R_{rs}&K_d error on derived a&b_b with the updated scheme.

Mean Error	R_{rs}(5%) K_d(0%)	R_{rs}(0%) K_d(5%)	R_{rs}(5%) K_d(5%)	R_{rs}(5%) K_d(−5%)	R_{rs}(10%) K_d(0%)	R_{rs}(0%) K_d(10%)	R_{rs}(10%) K_d(10%)	R_{rs}(10%) K_d(−10%)
a (%)	−0.7%	4.7%	4.0%	−5.5%	−1.4%	9.5%	7.9%	−10.9%
b_b (%)	4.2%	5.0%	9.4%	−1.1%	8.3%	10.0%	19.1%	−2.5%
Mean Error	R_{rs}(−5%) K_d(0%)	R_{rs}(0%) K_d(−5%)	R_{rs}(−5%) K_d(−5%)	R_{rs}(−5%) K_d(5%)	R_{rs}(−10%) K_d(0%)	R_{rs}(0%) K_d(−10%)	R_{rs}(−10%) K_d(−10%)	R_{rs}(−10%) K_d(10%)
a (%)	0.8%	−4.8%	−4.1%	5.6%	1.5%	−9.5%	−8.1%	11.3%
b_b (%)	−4.3%	−5.1%	−9.2%	0.5%	−8.7%	−10.2%	−18.2%	0.5%

The spectrum of particle backscattering coefficient (b_{bp}, m^{-1}) is generally considered following a power-law equation [36]

$$b_{bp}(\lambda) = b_{bp}(\lambda_0)\left(\tfrac{\lambda_0}{\lambda}\right)^{\eta} \qquad (6)$$

The spectrum of $b_{bp}(\lambda)$ was first calculated as $b_b(\lambda) - b_{bw}(\lambda)$, where $b_{bw}(\lambda)$ is the backscattering coefficients of pure seawater with values taken from Morel [34]. Further, η was calculated by a nonlinear fitting of $b_{bp}(\lambda)$ between 400 nm and 700 nm. For the simulation data set, the range of η of input $b_{bp}(\lambda)$ varies from − 0.5 to 2.5. Fig. 3 shows a histogram of the ratios of η calculated from retrieved $b_{bp}(\lambda)$ to those from known $b_{bp}(\lambda)$. It is found that the two η data sets agree with each other very well with the ratios ranging from 0.75 to 1.18 (mean value as 1.0). This result indicates that as long as r_{rs} and K_d are of high quality, it is adequate to obtain reliable hyperspectral b_{bp} from the hyperspectral measurements of r_{rs} and K_d.
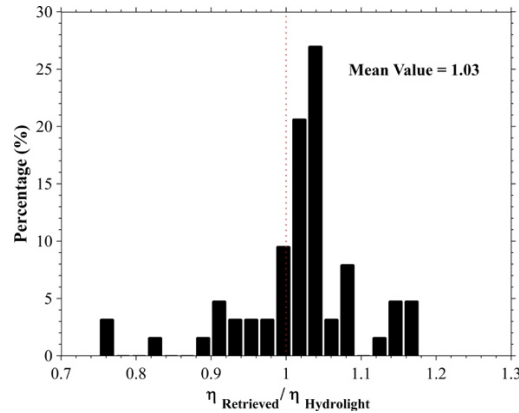

Fig. 3. A histogram of the ratios of η calculated from retrieved $b_{bp}(\lambda)$ to those calculated from Hydrolight-input $b_{bp}(\lambda)$.

4.2 Evaluation with field measurements

Further, hyperspectral data (Table 1) obtained from field measurements were used to evaluate the performance of the updated scheme. These include global measurements (NOMAD), measurements from VIIRS ocean color validation cruise in 2014 (VIIRS2014) and measurements collected in highly turbid inland water (Lake Taihu, China).

4.2.1 NOMAD

First, the NOMAD data set was used to evaluate the performance of the updated scheme. The data were collected in various waters covering a wide range of optical properties with a(490)

from ~0.01 to 2.0 m^{-1} [37]. An example of estimated and measured IOPs ($a(\lambda)$ and $b_b(\lambda)$) is shown in Fig. 4. It is found that good agreements were obtained between the estimates and measurements in the entire wavelength range of ~400 to ~670 nm, but b_b at ~683 nm is overestimated because of the contribution of chlorophyll-a fluorescence to r_{rs} at this wavelength, where no attempt (e.g., Huot et al. [38]) was taken here to remove this contribution in the process of deriving b_b.
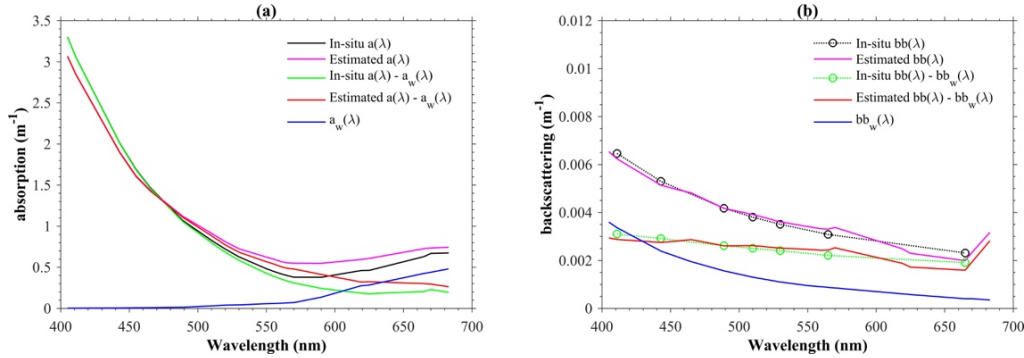

Fig. 4. An example of application to $R_{rs}(\lambda)$ and $K_d(\lambda)$ in NOMAD data set for retrieval of $a(\lambda)$ and $b_b(\lambda)$.
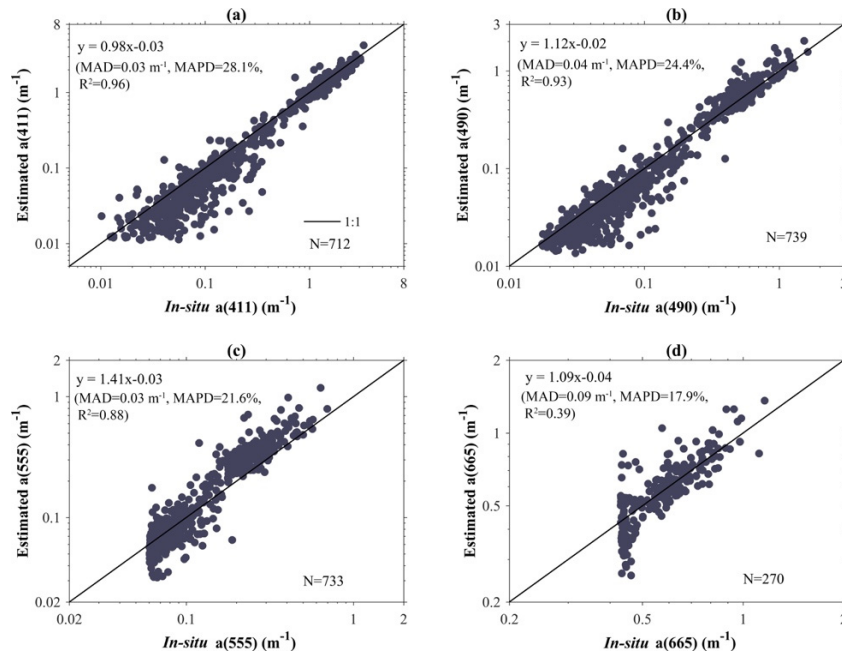
Fig. 5. Comparison (NOMAD data set) between *in situ* a and those derived from R_{rs} and K_d with the updated scheme.

Figure 5 shows a comparison of measured and estimated IOPs (a and b_b) at selected wavelengths (411, 490, 555 and 665 nm). The retrievals in general agree very well with those from *in situ* measurements. Taking 490 nm as an example, in linear regression analysis, a slope of 1.12 with an intercept of − 0.02 m^{-1} was obtained ($R^2 = 0.93$, N = 739) for $a(490)$, with a mean absolute deviation (MAD) of 0.04 m^{-1} and a MAPD of 24.4% (Fig. 5(b)). Separately, a slope of 0.95 and an intercept of 0.001 m^{-1} ($R^2 = 0.82$, MAD = 0.0007 m^{-1}, MAPD = 18.3%,N = 181) were obtained for $b_b(490)$ (Fig. 6(b)). In view both *in situ* measurements and derivation from AOPs have errors/uncertainties, these results suggest that

the a and b_b values derived from the combination of R_{rs} and K_d match well with instrument measurements.
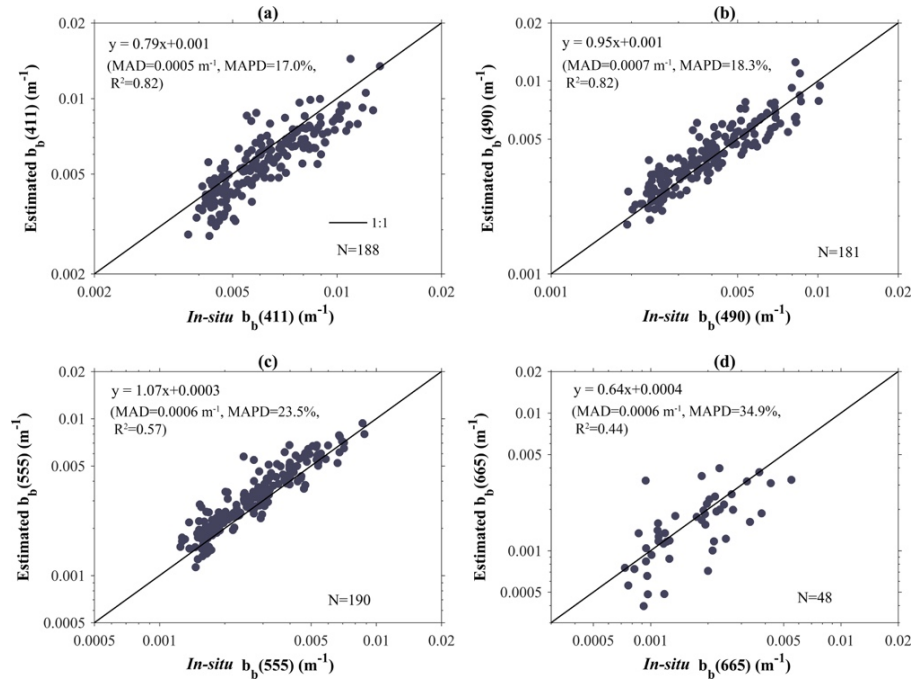

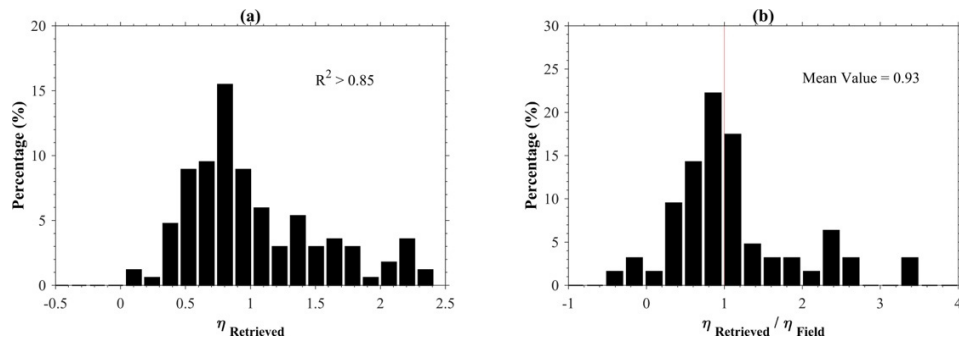Fig. 6. As Fig. 5, but for b_b based on the NOMAD data set.

Fig. 7. (a) Distribution of the retrieved η with fitting determination coefficient (R^2) higher than 0.85 (NOMAD data set); (b) Histogram of the ratios of retrieved η to those calculated from field $b_{bp}(\lambda)$ (all data points included).

The power-law formula (Eq. (6)) is still generally adopted by the community to describe the spectral variation of b_{bp} [7], although other schemes were also proposed [39]. The parameter η in Eq. (6) is important in ocean color remote sensing in many aspects, as it is required in inversion algorithms [5, 40, 41] and it is an indicator of particle size distributions [11, 12], but there has been limited reporting in the literature regarding its range and its variation for different waters or particulates. As a consequence, crude estimates have to be employed in ocean color algorithms in order to extend the analytically-derived b_{bp} at one wavelength (λ_0) to the rest of the visible bands [5]. Here, to evaluate the robustness of Eq. (6) for $b_{bp}(\lambda)$, nonlinear regression was carried out between $b_{bp}(\lambda)$ and λ (resulting slope is η) for *in situ* R_{rs}&K_d derived hyperspectral $b_{bp}(\lambda)$. The wavelength range is ~400 - 670 nm, thus avoiding the impact of chlorophyll-a fluorescence around 683 nm. It is found that more than ~83% of the waters studied have $R^2 > 0.85$ from this nonlinear regression analysis. Such a

result echoes that Eq. (6) is in general quite reliable in describing the spectral dependence of b_{bp} [36], although there are exceptions (~5% of this data set with R^2 less than 0.5). Further, it is found that the derived η ($R^2 > 0.85$) of this data set is in a range of ~0 – 2.4 and centered ~0.8 (Fig. 7(a)), with smaller (~0) values for coastal turbid waters and higher (~1.5 – 2.4) values for clear oceanic waters. Such a range of η is generally consistent with historical perceptions regarding the range of this property [42], but narrower than the range presented in Kostadinov et al. [12], especially for clear oceanic waters. Further, a histogram of the ratios of all retrieved η from R_{rs}&K_d to those calculated from field-measured $b_{bp}(\lambda)$ is shown in Fig. 7(b), and it is found that there are more than 80% of the points have the ratio within the range of ~0.5 - 1.5 (with a mean value as 0.93). Such results further support the use of hyperspectral R_{rs}&K_d for the derivation of hyperspectral b_{bp}.

4.2.2 VIIRS2014
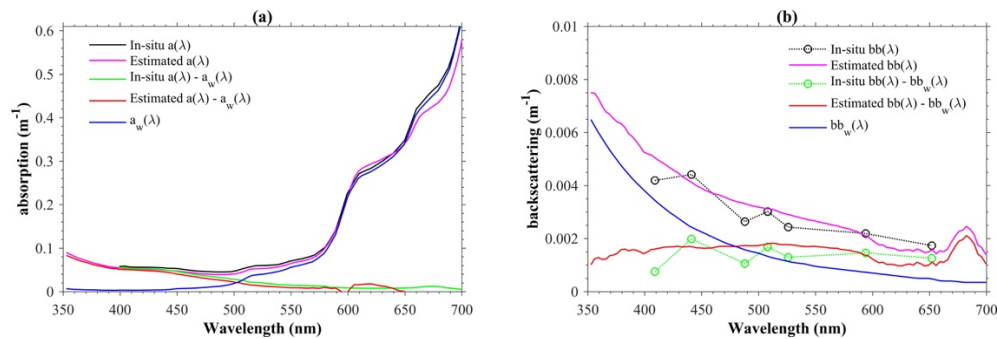
Fig. 8. As Fig. 4, but for the VIIRS2014 data set.

Further, a and b_b values were also estimated by the updated scheme from the measured K_d and r_{rs} of the VIIRS2014 data set. Because multiple-cast measurements were collected at each station, here we only used averaged values of these measurements and estimates for scheme evaluation and comparisons. Similarly, Fig. 8 shows an example of estimated and measured a and b_b spectra. It is found that the spectral features of $a(\lambda)$ and $b_b(\lambda)$ can be retrieved well by the new scheme. In particular, with this new scheme, the a and b_b values in UV wavelengths can also be estimated, while it is not possible to measure these yet with current commercial instruments (e.g., ACS, BB9).
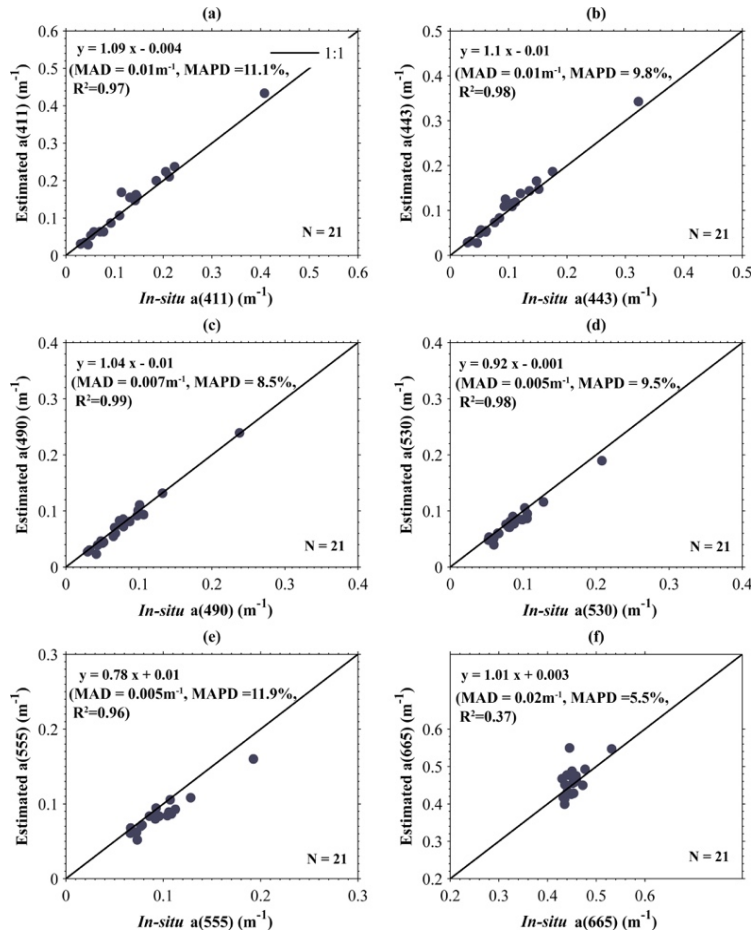
Fig. 9. ACS-measured *a* (VIIRS2014 data set) compared with those derived from r_{rs} and K_d.

Figure 9 shows a comparison of ACS-measured *a* with those derived from K_d and r_{rs} at selective wavelengths. Excellent agreements between the two independent determinations can be found where there are low MAD and low MAPD values (e.g., *a*(490) has MAD = 0.007 m^{-1} and MAPD = 8.5%). Larger uncertainties were observed at 665 nm, which is likely due to contributions of chlorophyll fluoresces at this wavelength, but the MAPD is still smaller than 6%. Likely in part due to more careful data processing and quality control, the agreement between the derived *a* and ACS-measured *a* is much better than that showing in the NOMAD data set. Figure 10 shows a comparison of BB9-measured $b_b(\lambda)$ and the retrievals from r_{rs} and K_d. For all wavelengths from 411 nm to 665 nm, a very good agreement was obtained where MAD is commonly less than 0.001 m^{-1} and MAPD < 30%. These results further demonstrate a robust performance of this updated scheme.
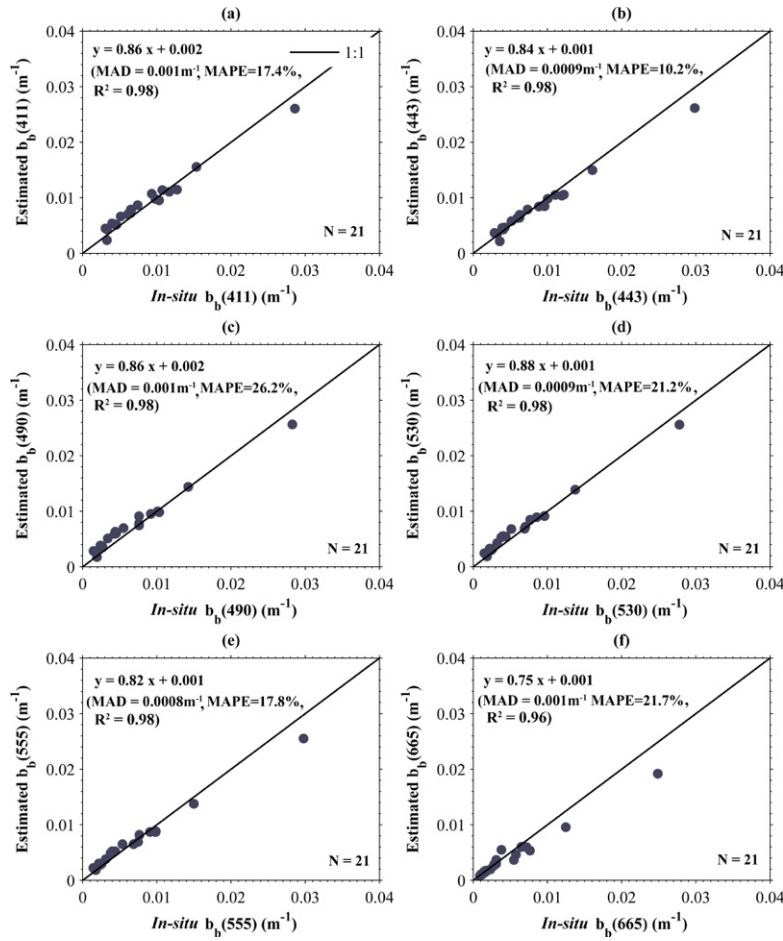
Fig. 10. As Fig. 9 but for b_b based on the VIIRS2014 data set.

Similarly, the range of the retrieved η based on r_{rs}-K_d derived $b_{bp}(\lambda)$ is found to vary from − 0.2 to 1.1 (Fig. 11(a)) with a mean value of ~0.55, which is consistent with the general nature that most of the stations are nearshore. Further, a histogram of the ratio of estimated η to that calculated from BB9-measured $b_{bp}(\lambda)$ is shown in Fig. 11(b), where ~75% of the ratios are within the range of 0.5 − 1.5 (average is 0.91).
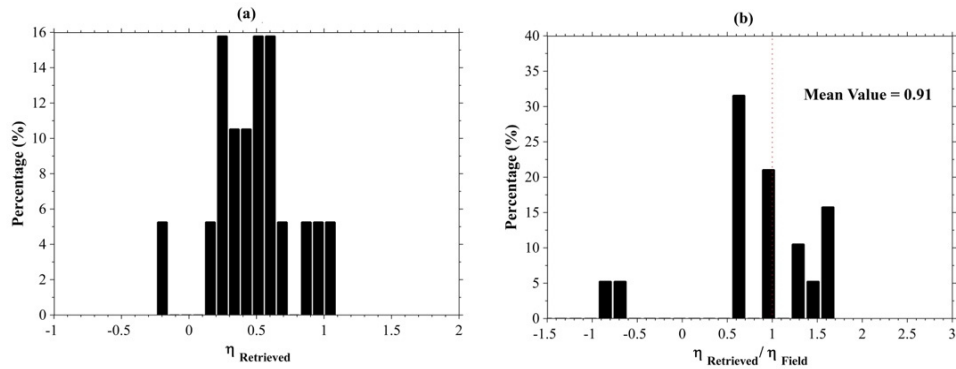
Fig. 11. As Fig. 7, but for the VIIRS2014 data.
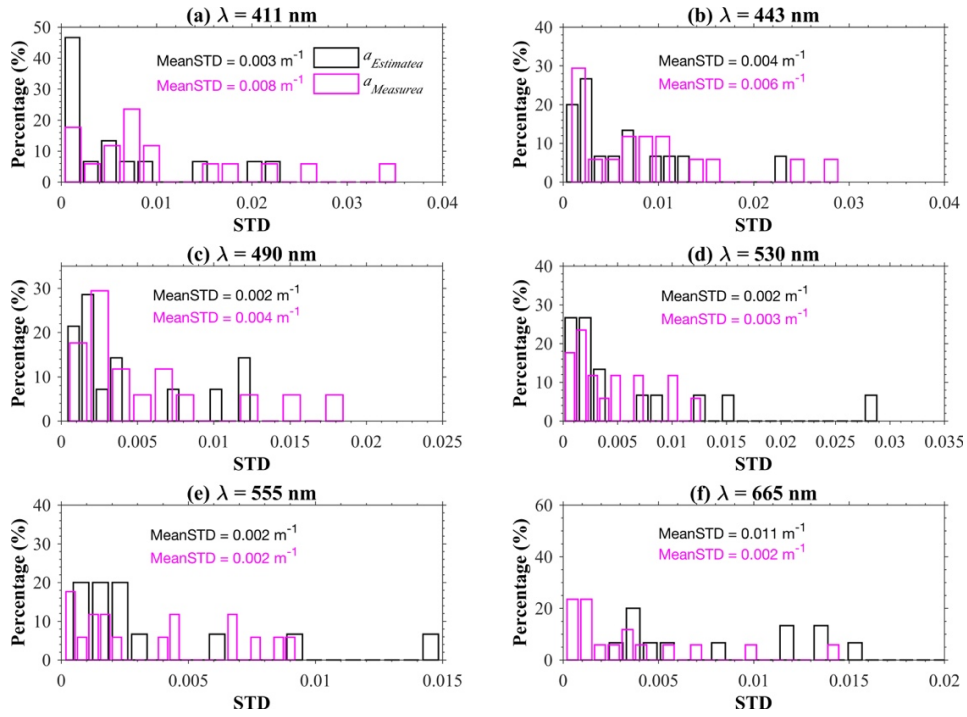
Fig. 12. Histograms of the standard deviation (STD) for total absorption coefficients estimated from multicasts of $E_d(z)$ and $L_u(z)$ (black bar) and those measured by ACS meters (magenta bar).
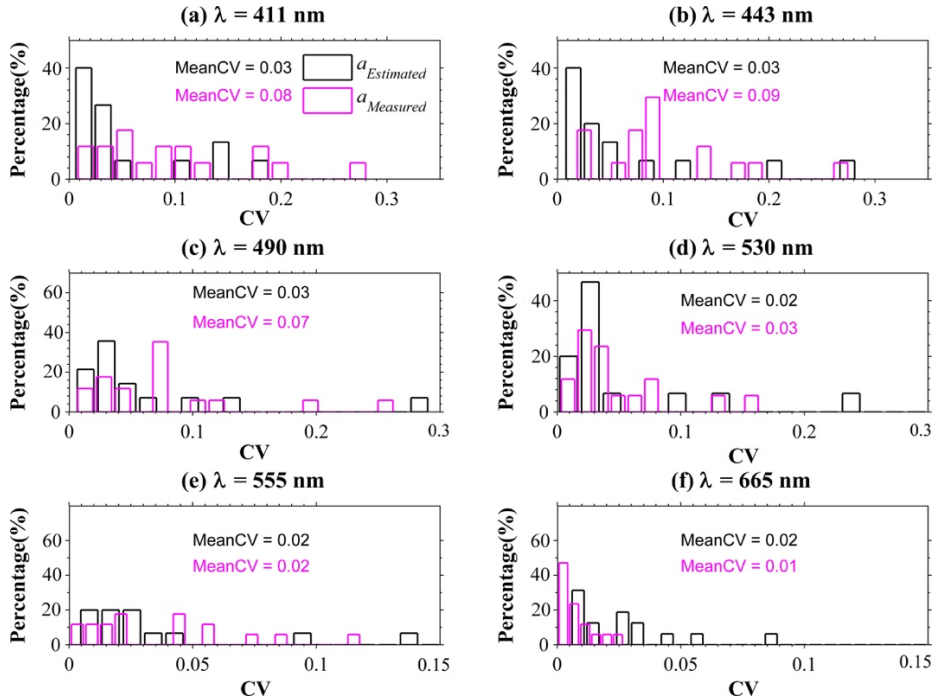

Fig. 13. Similar as Fig. 12 but for the coefficient of variation (CV).

With multicast measurements of E_d(z) and L_u(z), the standard deviation (STD) of $a(\lambda)$ estimated from r_{rs}-K_d is assessed, which are further compared with the STD of $a(\lambda)$ obtained from multicasts of ACS measurements. Note that because K_d is an average value in the upper water column, we here used the mean ACS-$a(\lambda)$ between 0^- and $z_{10\%}$ for comparisons. Figure 12 shows the histograms of STD for these determinations. For the wavelengths ranging from 411 to 555 nm, the STD of R_{rs}-K_d estimates is equivalent or smaller than that of the ACS measurements (at least for the data set evaluated). Taking 411 nm as an example, the STD of R_{rs}-K_d estimated $a(411)$ varies from ~0.001 to ~0.022 m^{-1} with a mean value as 0.003 m^{-1}, but the ACS-measured $a(411)$ had a range of ~0.001 to ~0.034 m^{-1} with a mean value as 0.008 m^{-1}, indicating a more reliable a was estimated from the combination of R_{rs} and K_d for this data set. Similarly, Fig. 13 shows the histograms of the coefficient of variation (CV) for these determinations, where CV is defined as the ratio of STD to mean value. We obtained similar results that the CV of R_{rs}-K_d estimates is equivalent or smaller than that of the ACS measurements. The higher STD (or CV) of ACS measurements could result from the processes involved with the pure-water calibration and/or the scattering correction. These issues have been widely reported and investigated in the last decades [9, 43, 44].
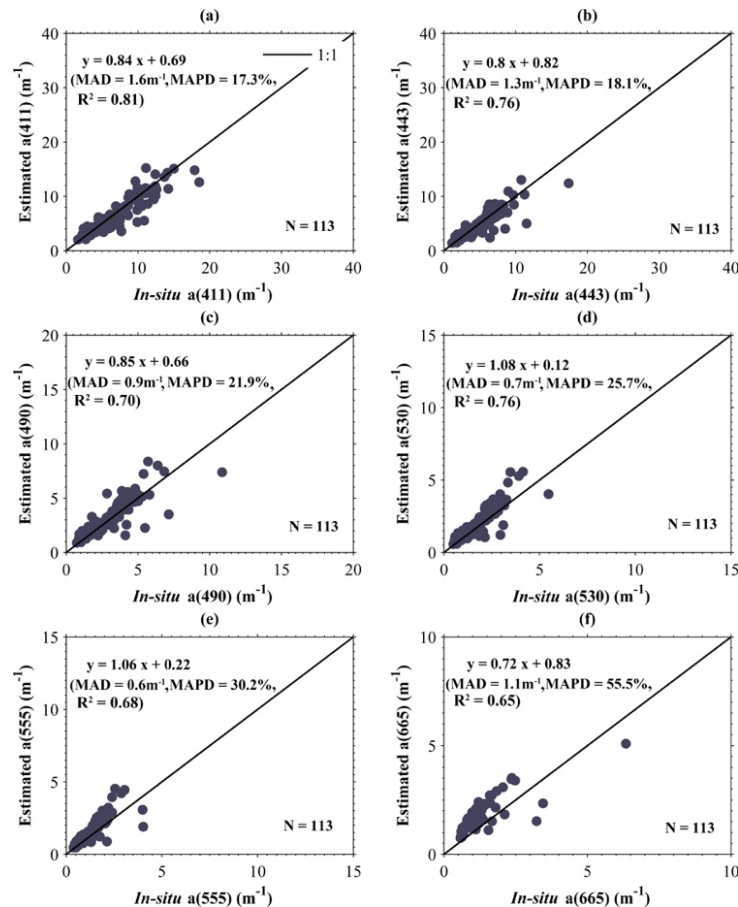
4.2.3 Lake Taihu

Fig. 14. Measured a (Lake Taihu data set) compared with those derived from R_{rs} and K_d.

Finally, the new scheme was evaluated with the measurements collected in Lake Taihu, China, where the optical properties are more complicated due to the highly dynamic environment (e.g., sediment resuspension due to wind and waves [45], complex network of

rivers or channels, and rich terrestrial input [46]). Figure 14 shows a comparison of measured and estimated a at selected wavelengths (411, 443, 490, 530, 555, and 665 nm). Although extremely high absorption coefficients were observed in this turbid water (a(443) can be as high as ~20 m^{-1}, for instance, see Fig. 14(b)), the two sets of a values (measured and retrieved a) agree with each other well (e.g., MAD = 1.3 m^{-1}, MAPD = 18.1% for a(443), see Fig. 14(b)). These results provide us further confidence in applying this updated scheme to obtain important IOPs even for extremely turbid waters.

5. Comparison with other approaches

The concept of deriving IOPs from a combination of AOPs is not new, where many previous studies [17, 18, 47–49] combined irradiance reflectance (R) and K_d for the derivation of absorption and backscattering coefficients, but R is seldom measured in the field anymore. We here briefly compare the results of the R_{rs}-K_d scheme with those of the two earlier R-K_d approaches [18, 47], as these approaches can be more easily implemented than other similar approaches [17, 48, 49]. The approach of Loisel and Stramski [18] was developed based on radiative transfer simulations, with much simpler relationships between IOPs and R (or K_d) compared to the approach of Morel [47]. We first evaluated the R-K_d approaches with the same data of r_{rs} and K_d calculated from the Hydrolight simulations, where a simple relationship ($R = 3.5\ r_{rs}$) was used to convert r_{rs} to R. Figure 15 shows a comparison of estimated a and b_b with the Hydrolight-input a and b_b. As indicated in Loisel and Stramski [18], the a can be well retrieved with a small MAPD (4.76%), while the b_b was generally overestimated for b_b lower than ~0.002 m^{-1} and underestimated for b_b higher than ~0.004 m^{-1}. The reasons for such (small) discrepancies may include the imprecise empirical conversion from r_{rs} to R and/or the approximations in the models between b_b and R (or K_d). For the approach of Morel [47], as simple relationships between IOPs and R (or K_d) were adopted, both a and b_b were estimated with relatively larger MAPDs (> 13%). In particular, most of the absorption coefficients were overestimated (Fig. 15(c)).
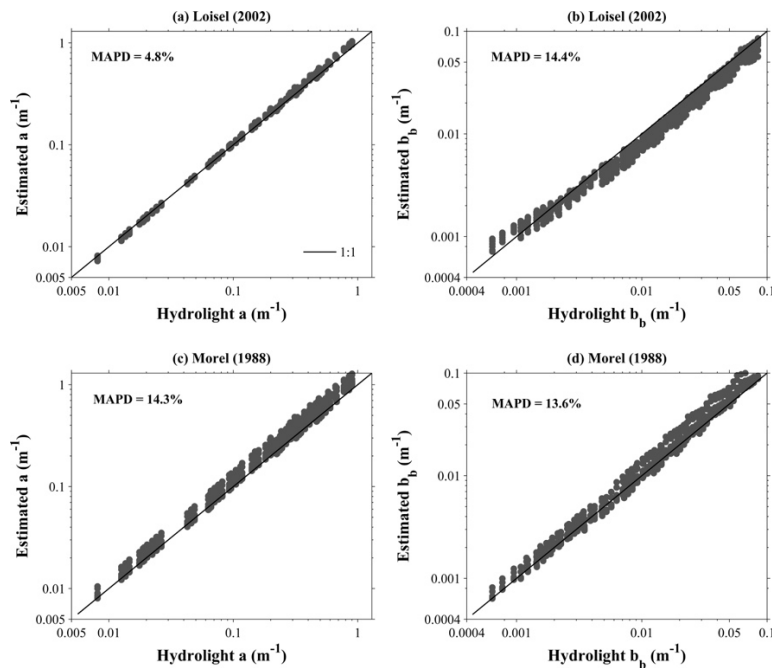

Fig. 15. Comparison of other two approaches [18, 47] for estimation of a and b_b with the same data of r_{rs} and K_d calculated from Hydrolight simulations.
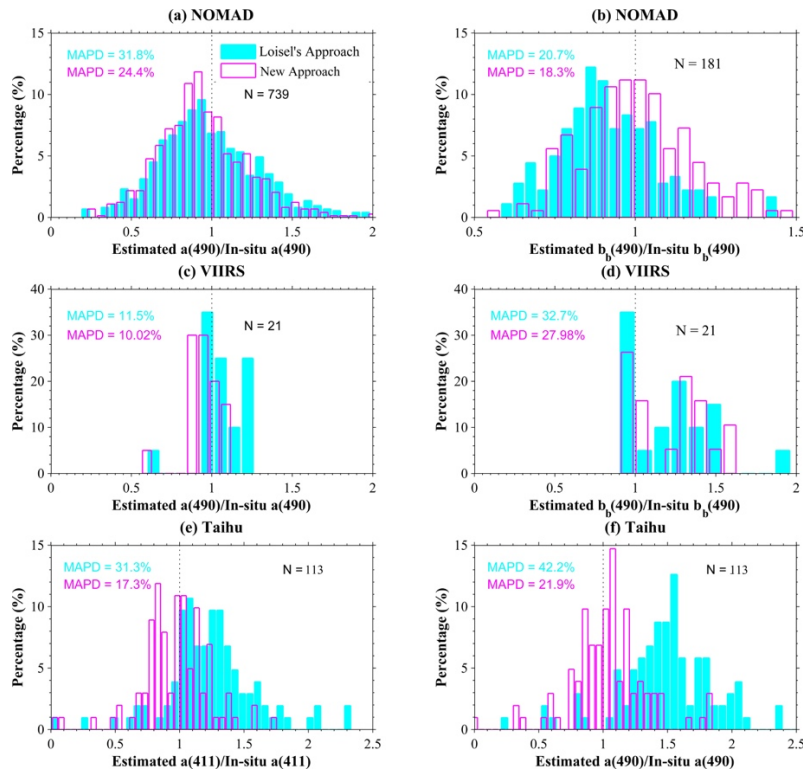
Fig. 16. Comparison of the approach of Loisel [18] with the updated scheme for estimation of IOPs with NOMAD, VIIRS2014, and Taihu data sets, respectively.

For field measurements, Fig. 16 shows histograms of the ratio of estimated $a(490)$ and $b_b(490)$ to *in situ* measurements. For the NOMAD data set, the approach of Loisel and Stramski [18] obtained similar $a(490)$ estimates when compared with the R_{rs}-K_d scheme (Fig. 16(a)), but more $b_b(490)$ are underestimated (Fig. 16(b)). For the VIIRS2014 data set, where most of the measurements were collected in coastal waters, both approaches obtained similar estimates (only limited data points available, N = 21). For the Lake Taihu data set, since there were no measurements of backscattering coefficients in this turbid water, comparisons are made regarding the absorption coefficients only. In such a turbid region, the R_{rs}-K_d scheme appears to derive more reliable $a(411)$ and $a(490)$ than the approach of Loisel and Stramski [18] (Figs. 16(e-f)). Similarly, Fig. 17 compares the R_{rs}-K_d scheme with the approach of Morel [47]. Generally, both $a(490)$ and $b_b(490)$ were overestimated when estimated with the R-K_d approach of Morel [47].
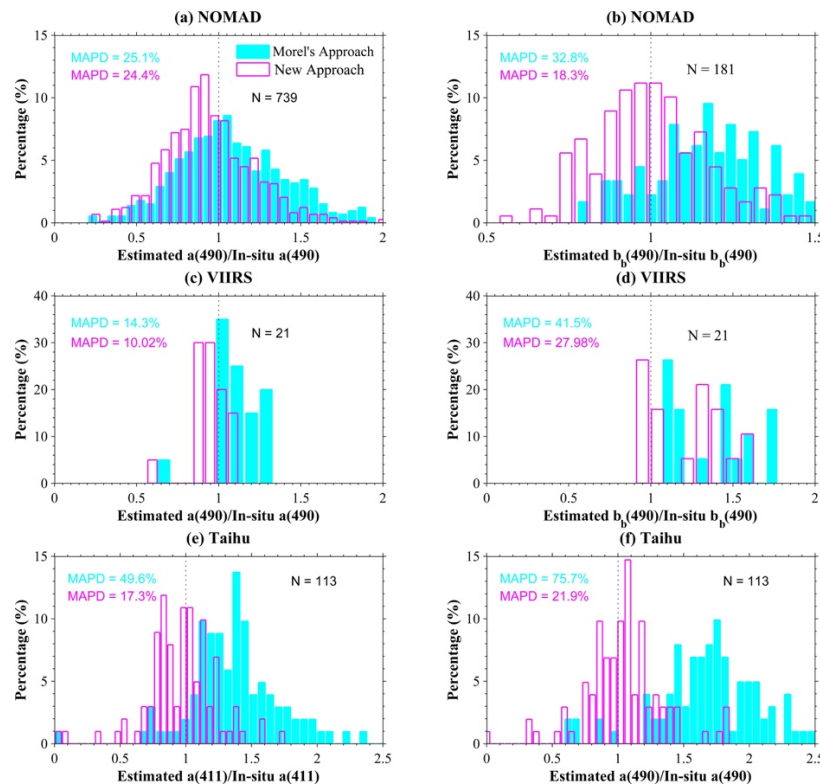
Fig. 17. As Fig. 16, but for the approach of Morel [47].

6. Discussions

Oceanography is a science where field measurements are critical to describe not only the spatial-temporal variations of various physical and biogeochemical properties, but also to understand the relationships and processes associated with such changes. This is also true for the inherent optical properties of the bulk waters, and it is always desirable to obtain these properties directly from proven instruments. For such, a few optical instruments (e.g., ACS, ECO-BB) are now widely used in the field to obtain information of water's IOPs (e.g., a and b_b). During ship-based surveys, these instruments can be employed in either profile or underway mode to provide data of high vertical or horizontal resolutions, therefore there have been lots of measurements of world oceans (especially those by AC9 or ACS) in the past decades.

However, it is necessary to keep in mind that these data are associated with various level of uncertainties inherent in the measurement strategy. In addition to the requirement of absolute calibration for the ACS or AC9 system that is not easy to perform accurately for clear oceanic waters (low optical properties approaching present instrument precision), a key aspect is that the direct measurements from these instruments are never IOPs, rather attenuated or scattered light intensities, where IOPs are calculated from these light signals. For instance, for the AC9 or ACS systems, the absorption (a) and the beam attenuation (c) coefficients are calculated based on light intensities measured at the two sides of the tubes holding the water samples. In particular, the calculation of a depends on a correction of the scattered signals in the tube for the measurement of a. Inevitably, for such calculations, assumptions and models (empirical or semi-empirical) have to be developed [8, 50]. These assumptions and models will introduce various levels of uncertainties to the final desired properties [9, 51]. Especially, as discussed in detail in a series of articles [52–54], a major challenge in the AC9 or ACS system for the 'measurement' of a is the correction of the

scattering contaminations. Various schemes have been developed for such corrections [8, 9, 43] with varying performances found for different waters. Uncertainties in the obtained a can be up to 80% [9].

On the other hand, the present b_b sensors (e.g., HS6, ECO-BB) never provide direct measurements of b_b, and are at a few spectral bands only. These b_b sensors not only just measure light scattered by water samples, but also at a fixed angle (varying from 120° to 140° for different instruments) that provides information for the determination of the volume scattering function (VSF, β, m^{-1} sr^{-1}) at this angle. It is then necessary to use models to correct the contaminations due to light absorption and scattering [55, 56] and then to convert this β at an angle to b_b [57, 58]. Because of these models and assumptions, uncertainties of the 'measured' b_b can easily be ~20% [55]. These practices and observations advocate the development of more robust instruments to accurately 'measure' IOPs *in situ* [59].

Similarly as the systems for *in situ* IOPs, the AOPs to IOPs schemes (including the updated R_{rs}-K_d scheme described here) do not provide a direct measurement of IOPs, rather they calculate IOPs based on models and assumptions using AOPs as inputs. Consequently, the accuracy of the derived IOPs depends on 1) accuracy of the AOPs, and 2) robustness of the assumptions and models used in the IOPs-AOPs relationships (e.g., no polarization included in current numerical simulations, etc.). Presently with the advancement of optical-electronic systems, as long as proper procedures and protocols are followed for instrument calibrations, hyperspectral upwelling radiance and downwelling irradiance in the water column can be measured well in the field. However, due to wave-introduced motions, these measured signals could be contaminated by sensor tilting and wave focusing/de-focusing [31, 60]. Although significant progress has been achieved in deriving both r_{rs} and K_d from such data [61, 62], it is still an ongoing research subject to improve the data quality of r_{rs} and K_d obtained from such profiling measurements [63, 64].

The errors or uncertainties in r_{rs} and K_d directly affect the accuracy of a&b_b derived from the R_{rs}-K_d scheme (see Table 3), but they have different impacts on the derived a and b_b values. Specifically, because K_d is primarily a sum of a and b_b [13, 65] and generally $a >> b_b$ for most natural waters, the accuracy of K_d has more impact on the accuracy of a; on the other hand, since r_{rs} is proportional to b_b, the accuracy of r_{rs} has stronger impact to the derived b_b. Also, as indicated in the *in situ* measurement of b_b where assumptions have to be made in order to convert single angle β to b_b, it is also required to assume a particle scattering phase function for the relationship between r_{rs} and IOPs [15, 16]. The uncertainty due to this assumption is found to be < 20% for most waters [16], and some closure studies have shown that the r_{rs} can be well reconstructed from *in situ* IOPs (a and b_b) if an appropriate phase function is used [66–68]. It is thus clear that inherently there will be some uncertainties between the *in situ* measured b_b and the R_{rs}&K_d derived b_b, because both systems actually obtain β at an angle (and not necessarily the same angle) and both have to assume some kind of phase function (again, not necessarily the same) in order to convert β at an angle to b_b. In view of the above, and keep in mind that many times during field measurements the waters targeted by R_{rs}&K_d were not concurrent with those targeted by the IOPs instruments or those used to get component IOPs (e.g., the particulate absorption coefficients included in NOMAD), the less than ~20% difference in a values (except Lake Taihu) and less than ~30% in b_b values between those derived from R_{rs}&K_d and those from IOPs instruments indicate excellent agreements from the two independent determinations. More importantly, even with the various sources of uncertainties associated with the R_{rs}&K_d system, the precisions of IOPs derived from the R_{rs}&K_d system are equivalent with the precisions of IOPs obtained from the present IOPs instruments (see Figs. 12-13). These results further support the generation of a&b_b with the R_{rs}&K_d system, where the latter could be further improved in the future with more realistic numerical models for aquatic environments [2, 25] and better understanding and determination of particle scattering phase functions [69].

Note that here the $R_{rs}\&K_d$ system aims at a well-mixed upper water column, and it does not produce depth-resolved solutions. If the upper water column is stratified, the derived $a\&b_b$ should be compared with averages in the upper water column (normally between 0- and $z_{10\%}$, as presented in this study) and larger uncertainties would be expected as the models of R_{rs} and K_d are based on vertically mixed waters. For stratified waters, a solution of the depth-dependent radiance-irradiance field is likely required in order to get depth-resolved IOPs as demonstrated in Gordon and Boynton [17] and Gordon et al. [70].

7. Summary

An updated scheme is presented in this study to derive a and b_b of bulk water from a combination of field-measured R_{rs} and K_d. Applications to both Hydrolight simulations and field measurements show that the retrieved a and b_b values match known or measured values very well for both clear oceanic waters and turbid coastal/inland waters. In particular, an analysis about product precisions indicates that the a and b_b values obtained from the $R_{rs}\&K_d$ system have equivalent precisions compared to those from present IOPs instruments, at least for data sets in this study. Therefore, with the existence of large AOP data sets, the updated $R_{rs}\&K_d$ system here not only provides an alternative and robust way to obtain $a\&b_b$ where there might be no measurements of such data from IOPs instruments, and the derived IOPs will be important and useful for studies of remote sensing and biogeochemical processes in the aquatic environments. More importantly, with hyperspectral R_{rs} and K_d, this scheme will fill the gap that the current b_b sensors cannot provide a measurement of hyperspectral b_b. On the other hand, it is always desired to have more robust instruments to measure hyperspectral IOPs *in situ*.